EXPERIMENTAL AND NUMERICAL STUDY OF THE FLOW IN A SYNTHETIC AORTA FOR TRAUMATIC RUPTURE CONDITIONS

William Craig Eberhardt, Sang Lee, Joseph A. C. Humphrey and Richard Kent
Department of Mechanical and Aerospace Engineering,
University of Virginia
122 Engineer's Way, Charlottesville, Virginia, 22904 USA
wce7a@virginia.edu, jach@virginia.edu, sanglee@virginia.edu, rwk3c@virginia.edu

ABSTRACT

Traumatic aorta rupture accounts for a large number of fatalities in automobile crashes. Conditions corresponding to aorta rupture are difficult to reproduce experimentally in simulated collisions involving cadaveric surrogates. As a consequence, *in situ* observations of the dynamics of the flow inside the aorta, and of the dynamics of the aorta structure itself, under suddenly imposed large pressure loads are virtually non-existent. This paper communicates a combined experimental and numerical investigation of the problem. An experimental model of an aorta, devoid of secondary arteries, has been constructed from poly(dimethylsiloxane) or PDMS. The synthetic aorta (SA) is U-shaped, having nominal: inside diameter of 20 mm; wall thickness of 2 mm; radius of curvature of 27 mm; inlet and exit tangent lengths of 80 mm and 160 mm. The SA is filled with water and immersed in a tank with flat, transparent Plexiglass walls, also filled with water. Both ends of the SA are securely attached to fixed, vertical metal tubes. One tube is connected to an airtight overhead tank filled with water, and the other has a needle valve attached to its end. For the experiments communicated here, the needle valve is kept closed. The free surface of the water in the overhead tank is sequentially pressurized and depressurized very quickly to simulate the time-dependent pressure load associated with traumatic aorta rupture conditions. Observations of the flow in the SA via Particle Image Velocimetry (PIV), are obtained for a range of relevant dynamical conditions. The experimental observations are found to be in good agreement with corresponding numerical calculations obtained using ANSYS. This allows the use of the code to explore more realistic geometries and dynamical conditions relevant to traumatic aorta rupture and beyond the range of the experiments. The paper presents and discusses some of the most interesting findings.

INTRODUCTION

Epidemiology and Anatomy

Aortic injury continues to be a leading cause of automotive mortality, occurring in about 20% of motor vehicle accidents (Katyal et al., 1997 and Richens et al., 2002). Since the aorta is the main artery conveying oxygenated blood, its rupture constitutes a severe injury with about 90 percent of victims dying at the crash scene (Symbas et al., 1973). A detailed understanding of the injury mechanism of traumatic aorta rupture (TAR) is necessary to increase survival rate.

With reference to Fig. 1, the aorta commences at the aortic root which exits the heart superiorly at the left ventricle. It ascends the thorax superiorly, arches posteriorly to the left side and descends within the thorax on the left side of the vertebral column. The diameter of the aorta decreases from the root (approx. 25mm) to the iliac bifurcation (approx. 18mm). The primary site of traumatic aorta rupture (TAR) in 75-85% of all cases is reported at the isthmus, which is a transition region between a relatively mobile heart and a relatively fixed descending aorta (Katyal et al., 1997 and Lundewall, 1964).

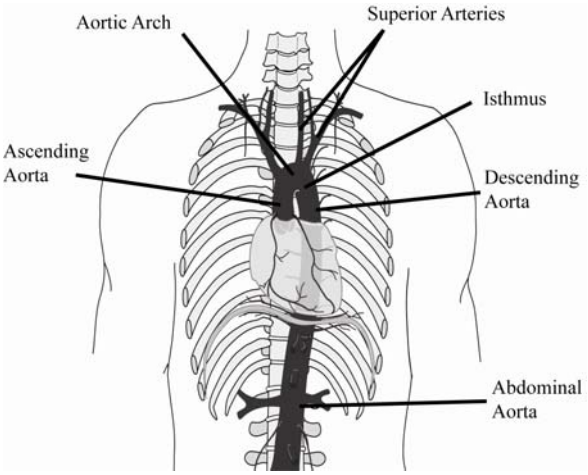

Fig. 1. Aorta anatomy

The Problem of Interest

The mechanism responsible for TAR remains unknown due to the difficulty of reproducing the physical phenomenon experimentally and theoretically. Several hypotheses have been proposed for TAR such as: (i) relative motion between the heart and the ascending aorta; (ii) water-hammer effects; and, (iii) osseous pinch (Lundewall, 1964; Crass et al., 1990; and Mohan and Melvin, 1982). A dynamic pressure pulse may also be a primary or contributory mechanism of TAR. The pressure increase is a result of the compression of the thoracic cavity causing blood to be forced out of the heart and down the aorta, or a result of restraint devices causing a pressure pulse to travel up the aorta towards the heart.

This study focuses on the pressure pulses traveling through a simplified physical model of the aorta in order to

reduce uncertainties inherent in the real, much more complex system. An experimental and numerical investigation is performed to elucidate the fluid mechanics and fluid-structure interactions associated with aorta rupture during imposed hyper-physiologic pressure loads.

Objectives

The objectives of this study are twofold: (1) to perform reproducible experiments elucidating aorta rupture in a synthetic aorta; (2) to develop and validate a coupled flow-structure computational model for aorta rupture. In this manner the flow and boundary condition complexities will be reduced allowing for a validated computer simulation that can then be used to analyze more complex geometries and flow patterns. Thus, this work aims to provide an accurate description of boundary conditions as well as fluid and solid material responses in a simplified PDMS aorta model which will lead to an improved understanding of TAR.

EXPERIMENTAL STUDY

Synthetic Aorta

In order to perform reproducible experiments and of simpler flows to be modeled through computer simulations (discussed below), the human aorta is modeled as a U-shaped tube of fixed circular cross-section (Fig. 2). The tube for the experiments is chosen to have an inner diameter of 21.4 mm and allows for easy installation in the test rig. The wall thickness is 2 mm, and the radius of curvature is 27 mm as measured from cadaver aortas. The straight sections of the tube have lengths of 80 and 160 mm. The tube is constructed from Slygard 184, a transparent PDMS silicone elastomer, from Dow Corning.

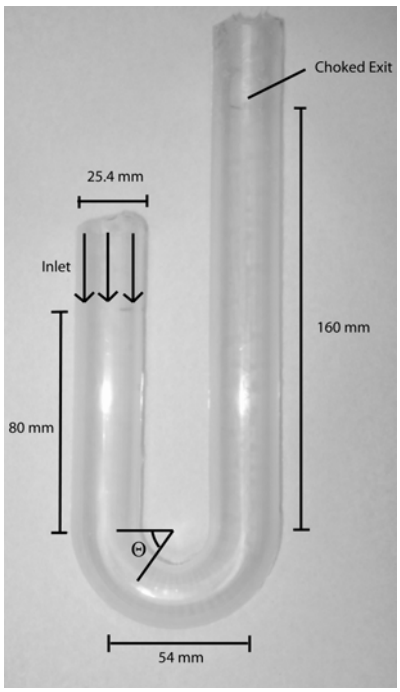

Fig. 2. SA dimensions and flow direction.

Test Rig

A schematic of the apparatus including the test section is provided in Fig. 3. The system is designed to produce repeatable pressure pulses similar to those measured in the aortas of cadavers during simulated crashes (Bass et al., 2001). The rig is capable of delivering pressures up to 10^6 Pascals, well above the range observed in TAR.

The molded PDMS tube is suspended upside down (Fig. 2) relative to its orientation in the human body. It is contained in a transparent rectangular plexiglass tank filled with water. This serves to simulate the physiology while reducing index of refraction effects. The longer straight section of the U-shaped PDMS tube is attached by a lined worm drive and tube clamp to a stainless-steel pipe terminating at a needle valve that allows for the control of the flow through the PDMS tube. The shorter straight section of the PDMS tube is attached to another stainless-steel pipe by a lined worm drive and tube clamp leading to a water reservoir tank above it. Attached to each side of the reservoir are half-inch (normally closed) solenoid valves. One valve exits to the environment and the other is attached to a pressure source. The pressure source is filled by an air compressor and then sealed off with a valve. The solenoid valves are controlled by a programmable delay that upon triggering activates the first valve allowing air to flow into the reservoir. After a set time the first valve is closed and the second is opened allowing the pressurized air to exit the system. In this manner a variety of pressure pulses can be imposed and accurately reproduced (Fig. 4).

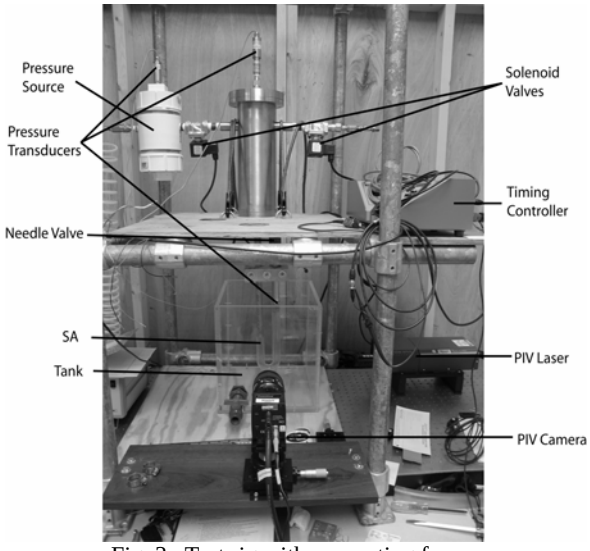

Fig. 3. Test rig with supporting frame.

Equipment and Experimental Methodology

The Particle Image Velocimetry (PIV) measurements of fluid velocity are conducted using a TSI Power View system. A combination of cylindrical and spherical lenses is used to focus the pulsed laser light sheets along the geometrical symmetry plane of the PDMS test section. The duration of each laser pulse is 3-5 ns and the time between pulses is set depending on the velocities induced by the imposed pressure pulse. A number of carefully timed images of the flow is captured and then processed using two frame cross correlations of 50 image pairs using a Gaussian

peak search algorithm through TSI Insight 4. The mean flow is obtained from the results of each measurement case. The data are smoothed and velocity vectors exceeding three standard deviations are removed. Hollow spherical glass particles of nominal diameter 8-12 μm and density 1500 kg/m^3 are used to seed the flow.

The pressure regulator and solenoid valve delays are set to produce the desired pressure pulses. For the PIV measurements, the test section is filled through the reservoir with water mixed with the hollow glass beads and any air is removed from the system except for a 20 cm layer of air at the top of the reservoir. The system is then submitted to the controlled pressure pulses (Fig. 4) during which PIV measurements can be made in the PDMS tube. Six segments of the tube (Fig. 5) are examined in separate tests to improve velocity vector resolution and accuracy. Fifty image pairs were taken for each section and the resulting velocity data were averaged.

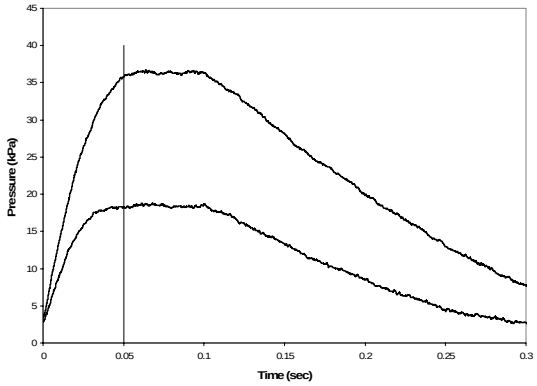

Fig. 4. Characteristic pressure pulses imparted to SA.

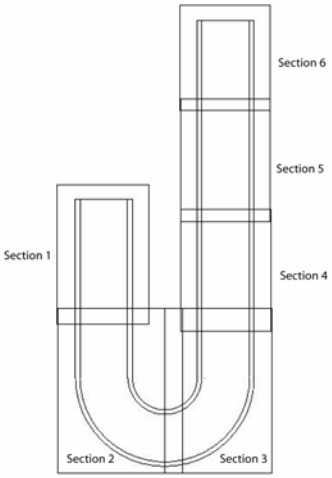

Fig. 5. Areas of SA examined with PIV.

Uncertainties

The molds used for the construction of the SA were milled from a Modela Pro MDX-650. This milling machine has a mechanical resolution of 0.001 mm/step and repeat accuracy of 0.05 mm (Roland). The hollow glass particles used to seed the flow have a theoretical Stokes drag-based relaxation time of less than 12 microseconds. This time is several orders of magnitude smaller than the characteristic flow time scale, thus rendering particle lag negligible.

The sources and magnitudes of uncertainties regarding PIV measurements have been documented in the literature (Raffell et al. 1998). In this work, the uncertainties pertaining to particle out-of-plane displacement, particle displacement in a sub region, and the time between laser pulses are negligible. Optical distortion created by the curvature of the SA is minimized by the fact that it is filled with water and placed in a water filled tank with flat walls. The laser light sheet is aligned to pass normally through the tank and through the symmetry axis of the SA. The camera is placed normal to the light sheet. The movement of the SA resulting from the pressure pulse is in-plane with the laser light sheet and the time between pulses is small enough to prevent significant velocity measurement error due to this deformation.

NUMERICAL STUDY

Fluid and Solid Phase Conservation Equations

For the purposes of this study, blood is considered to be a Newtonian fluid and its flow is described by the Navier-Stokes equation. Because the arbitrary Lagrangian-Eulerian (ALE) scheme is used to track moving surfaces at the interfaces between fluid and solid structure boundaries, the fluid phase continuity and momentum equations in component form are

$$u_{i,i} = 0$$

$$\rho u_{i,t} + \rho\left(u_j - \hat{u}_j\right)u_{i,j} = -p_{,j} + \tau_{ij,j} + \rho f_i \ \ in\ \Omega_F$$

where, u_i is a velocity component, p is pressure, ρ is fluid density, f_i is a body force component per unit mass, $\hat{u}_j$ is a structure velocity component.

The equations describing a deformable structure are represented by Cauchy's theorem and the equilibrium equation.

$$T_i = \sigma_{ij} n_j \ \ on\ \Gamma_S$$

$$\sigma_{ij,j} + \rho f_i = \rho a_i \ \ in\ \Omega_S$$

where, T_i is a component of the surface traction, σ_{ij} is a component of the Cauchy stress tensor, n_j is a component of the outward normal on the surface Γ_S, and a_i is a component of the acceleration vector.

For finite elastic deformations that are typically observed in biological tissues, the constitutive equation can be expressed by a strain-energy function.

$$W = \rho_0 e = W(\mathbf{F}) = W(\mathbf{C})$$

$$\sigma_{ij} = J F_{ij} \frac{\partial W}{\partial F_{ij}} \ \ and \ \ J = \det(\mathbf{F})$$

where, ρ_0 is the structure density in the reference configuration, e is the energy per unit mass, $\mathbf{F}$ is the deformation gradient tensor and $\mathbf{C}$ is the right Cauchy-Green tensor.

ANSYS and FSI Algorithm

The fluid-structure interaction was implemented by using ANSYS finite element package (ANSYS, Inc., Release 10.0). The coupling procedure is provided by automated iterations across two different fields, named the Multi-field solver. The physics of each domain is solved separately using the ANSYS Structure solver for the solid structure domain and ANSYS FLOTRAN for the fluid domain. The solution procedure transfers fluid forces to the structure and receives solid displacements while the stagger loop satisfies the convergence criteria. The algorithm continues to loop through the analyses until the global time condition is satisfied.

PDMS material characterization

The PDMS tube is assumed to be isotropic, incompressible and hyperelastic with a 5-parameter Mooney-Rivlin material model. The form of the strain energy function is given by

$$W = C_{10}(I_1 - 3) + C_{01}(I_2 - 3) + C_{20}(I_1 - 3)^2 + C_{11}(I_1 - 3)(I_2 - 3) + C_{02}(I_2 - 3)^2$$

in which, C_{ij} are the material constants and I_i are the strain invariants. The material properties are determined by curve fitting based on uniaxial extension tests (Scott, 2004) shown in Fig. 6. The material constants are provided in Table 1.

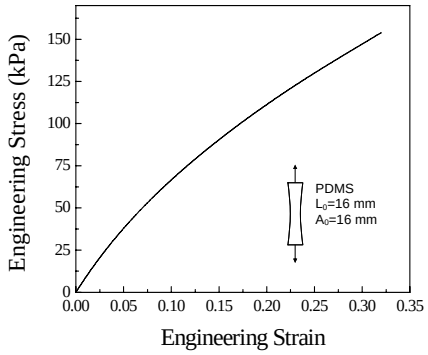

Fig. 6. Stress-strain curve from PDMS uniaxial extension test.

C_{10}	-265.28
C_{01}	414.39
C_{20}	501.94
C_{11}	-1441.2
C_{02}	1189.0

Table 1 Mooney-Rivlin material constants ($\times 10^3$)

Solution Methodology, Modeling and Simulation

A symmetric finite element model for the PDMS tube is built with respect to the X-Z plane (Fig. 6). The fluid domain is modeled with 8-node FLOTRAN CFD elements (FLUID142). Water properties at 20 °C (ρ = 997 kg/m^3, μ = 1.002×(10^{-3}) kg/m s^{-1}) are used. For cases with through flow along an aorta or a U-shaped tube, the flow may be turbulent due to the high levels of wall shear induced by a characteristic pressure pulse. Accordingly a standard k-ε turbulence model is used in the fluid analysis. For the PDMS tube itself, 8-node structure elements (SOLID185) are used. The geometric nonlinearity and stress-stiffness effects due to large deformations are considered for the structure analysis. The meshed model is shown in Fig. 7. The pressure pulses (Fig. 4) are applied at inlet (A) while the outlet (B) is defined to have zero fluid velocity to represent the effects of a closed valve. A non-slip velocity condition is imposed at the fluid boundaries interfacing with the PDMS wall. In each stagger loop, as the tube deforms, the fluid domain moves to satisfy the boundary conditions at the moving interfaces via ALE mesh morphing. The code has been previously validated by Lee et al. (2007).

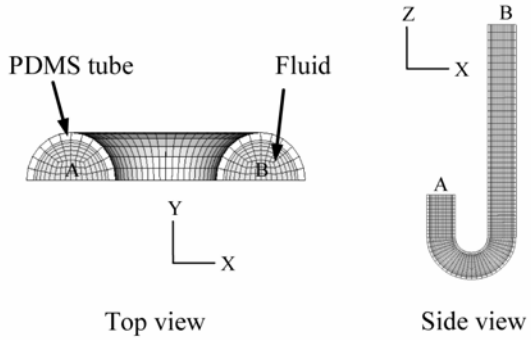

Fig. 7. SA finite element model.

RESULTS

Velocity

Contour plots of the velocity magnitude at 50 ms after the beginning of the pressure pulses are provided in Figs. 8 and 9. In these tests the needle valve was kept closed prohibiting any fluid from leaving the system. The flow of water into the SA is a direct result of the change in volume due to the pressure. The maximum velocities were located at the inlet in each test and the velocity reached zero at the end of the SA. The velocities ranged from roughly 1 m/s to 0 m/s for the larger pulse while the magnitude was about half that for the smaller pulse. The flow in the SA is characterized by large velocities over very short times resulting in relatively small SA wall displacements.

As expected from potential flow theory, between Θ = 45° and 90° in the arch region fluid motion is greater near the inner curve than the outer. This is demonstrated in Figs. 8 and 9. This region of increased velocity coincides with the location of the isthmus where TAR occurs. Figures 10 and 11 show velocity profiles at Θ = 0°, 90° and 180° in the arch.

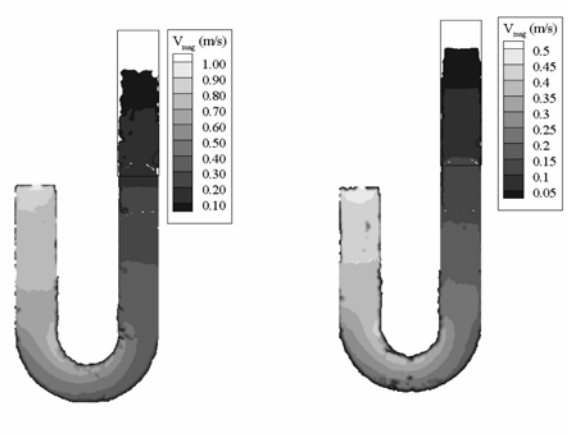

Fig. 8. Velocity contour of larger (left) and smaller (right) pressure pulses (measurements).

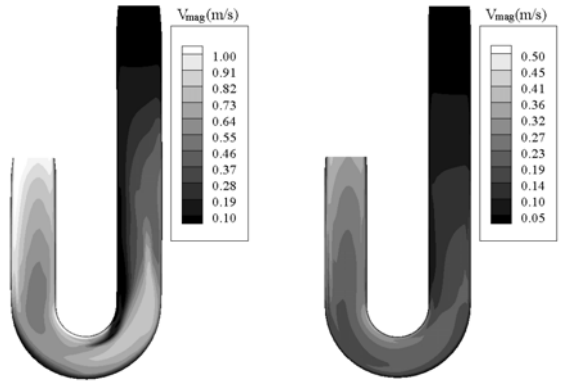

Fig. 9. Velocity contour of larger (left) and smaller (right) pressure pulses (calculations).

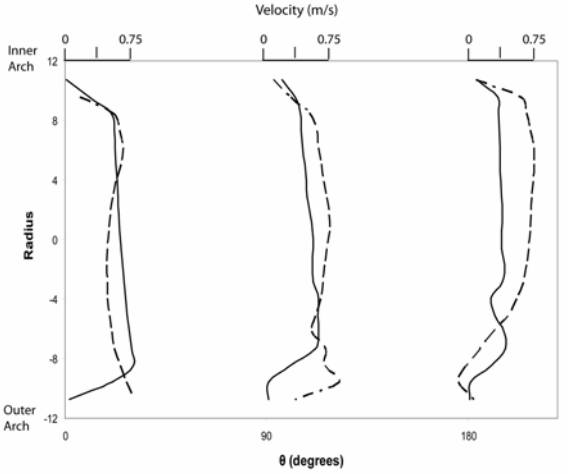

Fig. 10. Velocity profiles in SA arch for larger pulse (measurements: solid line, calculations: dashed line).

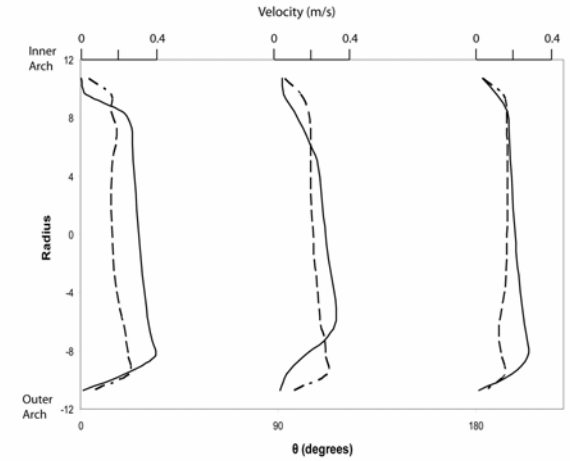

Fig. 11. Velocity profiles in SA arch for smaller pulse (measurements: solid line, calculations: dashed line).

Wall Deformation

The displacement of the tube at 50 ms into the larger pulse is shown in Fig. 12 with a 5× magnification factor. The maximum deformation occurs at the inner radius of the arch which matches observations in the experimental tests.

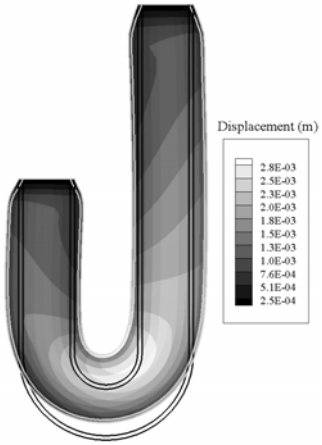

Fig. 12. Magnified SA deformation (calculations).

Pressure and Wall Shear Stress

The pressure and wall shear stress distributions along the inner and outer arch of the SA at 50ms are obtained from numerical calculation. To facilitate comparison, the pressure values for the two pulse cases are normalized by their maximum magnitudes ($P_{S,max}$ = 19.16 kPa, $P_{L,max}$ = 34.65 kPa). Although a nearly uniform pressure is observed throughout the SA in both cases, their distribution is reversed when the pressure causes moderate wall deformation (Fig. 13). The pressure distribution-wall deformation relation is currently under investigation.

The distribution of wall shear stress along the inner and outer wall is represented by the wall shear rate (WSR) in Fig. 14. The maximum WSR is consistently observed at the inner arch in both cases, which corresponds to the isthmus

region in the human aorta. It is remarkable that the increased pressure (by a factor of 1.81) and corresponding wall deformation result in a significant rise in the wall shear stress at the arch region (by a factor of 3.14).

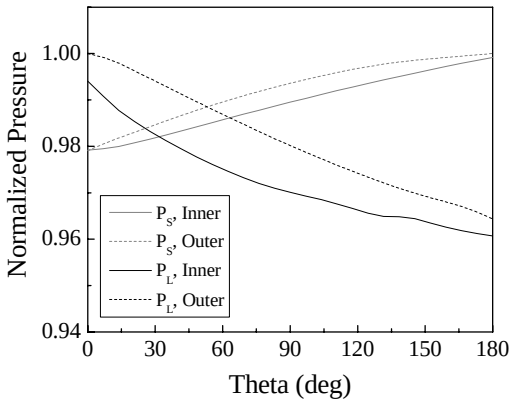

Fig. 13. Pressure distribution along the SA (calculations).

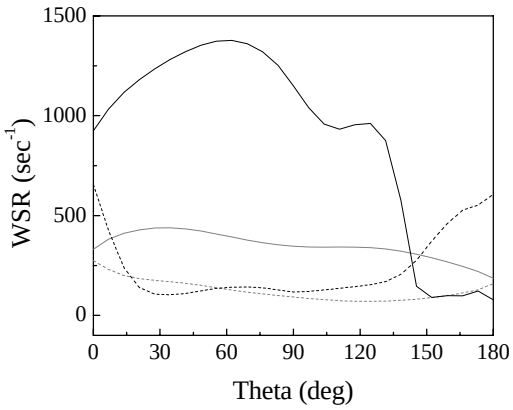

Fig. 14. Wall shear rate along the SA (calculations); same coding of plotted lines applies as in Fig. 13.

DISCUSSION

The results of this combined experimental and numerical study demonstrate the potential for algorithmic software to accurately calculate fluid flow in a nonlinear material undergoing deformation due to a suddenly imposed pressure pulse. Both the measurements and calculations reveal larger velocities and deformations at the inner radius of the aorta arch.

Differences between measured and calculated results of the velocity distributions at the SA inlet are attributed to differences in boundary conditions. In the experiment a straight pipe leads into the SA allowing for some degree of flow development prior to entering the curved section. The numerical simulation does not account for this effect.

Although, overall, measured and calculated shape and displacement trends of the SA match, the magnitude of the deformation is greater in the numerical calculation than in the experiment. This, again, is attributed to differing boundary conditions. The experimental SA is suspended in a tank of water resulting in forces on the outer wall and this condition is not represented in the calculations.

ACKNOWLEDGEMENTS

The authors thank M. Begley for his suggestions and technical guidance leading to the fabrication of the PDMS aorta. The use of the fabrication equipment in the laboratory of H. Bart-Smith, as well as helpful consultations with J. Bolton, of the Center for Applied Biomechanics, bearing on the final design and fabrication of the PDMS aorta are gratefully acknowledged. We are indebted to C. Barbier for valuable discussions and guidance relating to the use of the PIV instrumentation. This project is supported by the U.S. Department of Transportation, National Highway Traffic Safety Administration under Cooperative Award No. DTNH22-01-H-07292.

REFERENCES

Bass, C. R., Darvish, K., Bush, B., Crandall, J.R. (2001) "Material properties for modeling traumatic aortic rupture." *Stapp Car Crash Journal*, 45, 143-160

Bush, B. (2001) "Failure properties of human aortas," M.S. Thesis, University of Virginia, Charlottesville, VA, USA.

Crass, J. R., Cohen, A.M., Motta, A.O., Tomashefski, J.F., Wiesen, E.J. (1990) "A proposed new mechanism of traumatic aortic rupture: the osseous pinch." *Radiology*, 176, 645-649.

Forman, J., Kent, R., Bolton, J., and Evans, J. (2005) "A method for the experimental investigation of acceleration as a mechanism of aortic injury." *SAE Transactions*, Paper 2005-01-0295.

Katyal, D., McLellan, B.A., Brenneman, F.D., Boulanger, B.R., Sharkey, P.W., Waddell, J.P. (1997) "Lateral impact motor vehicle collisions: significant cause of blunt traumatic rupture of the thoracic aorta." *J. Trauma*, 42 (5), 769-772.

Lee, S., Humphrey, J., Kent, R. (2007) "Numerical modelling of fluid-structure interactions in cardiovascular mechanics." *Computer Methods in Biomechanics and Biomedical Engineering* (under review)

Lundewall, J. (1964) "The mechanics of traumatic rupture of the aorta." *Acta. Pathol. Microbiol. Scand.*, 62, 34-36.

Mohan, D., Melvin, J.W. (1982) "Failure properties of passive human aortic tissue I-Uniaxial tension tests." *J. Biomechanics*, 15(11), 887-902.

Raffel, M., Willert, C., and Kompenhans, J., 1998, *Particle Image Velocimetry-A Practical Guide*, Springer-Verlag, Berlin.

Richens, D., Field, M., K., Neale, M., Oakley, C. (2002) "The mechanism of injury in blunt traumatic rupture of the aorta." *Eur. J. Cardiothorac Surg.*, 21, 288-293.

Roland. *3D Milling Machine MDX-650*. Japan, 2002.

Scott, O. (2004) "Indentation to characterize films," M.S. Thesis, University of Virginia, Charlottesville, VA, USA

Symbas, P. N., Tyres, D.H., Ware, R.E. (1973) "Traumatic rupture of the aorta." *Ann. Surg.*, 178(1), 6-12